Stacking faults and alternate crystal structures for the shape-memory alloy NiTi

M. Krcmar[1,*] German D. Samolyuk,[2] and James R. Morris[3,†]

[1]*Department of Physics, Grand Valley State University, Allendale, Michigan 49401, USA*

[2]*Materials Science and Technology Division, Oak Ridge National Laboratory, Oak Ridge, Tennessee 37831-6115, USA*

[3]*Ames Laboratory, U.S. Department of Energy at Iowa State University, Ames, Iowa 50011-3020, USA*

(Received 18 January 2020; accepted 21 September 2020; published 12 October 2020)

We use *ab initio* calculations to study the role of stacking faults in connecting the high-temperature B2 and the theoretically predicted low-temperature B33 NiTi phases. In contrast with prior work, we describe the B2 → B33 phase transformation in terms of alternate bilayer shifts by $\frac{1}{2}$ [100] on the $(011)_{B2}$ plane, obtaining a viable pathway; the same mechanism could also work with the B19 parent phase. We then examine B33-like structures built from alternate stacking sequences of B19 bilayers, constructed to have monoclinic tilt angles close to the experimentally reported NiTi B19′ martensite, and find four low-energy stacking-fault variants with energies 5.8–8.5 meV/atom above the calculated B19′ martensite structure, suggesting that such structures might appear as a part of the NiTi martensite phase at low temperatures. Investigating further the occurrence of specific coordinated planar shifts in NiTi systems, we report a dynamically stable NiTi B27 phase and find that it is only 1.2 meV/atom above the calculated B33 ground-state structure, thus having a potential to also play a role in NiTi martensitic phase transformation.

DOI: 10.1103/PhysRevMaterials.4.103606

I. INTRODUCTION

Shape-memory nickel-titanium alloy phases and its martensitic phase transformation have been subjects of extensive theoretical [1–7] and experimental [8–13] investigations for decades. Renewed theoretical interest in recent years stems from still-disputed fundamental issues regarding associated structures and transition barriers for the martensitic phase transformation, accompanied with ever-increasing computational abilities which now allow investigations of a wide spectrum of possible transition pathways, as well as finite-temperature properties by methods which incorporate first-principles calculations together with fundamentals of statistical thermodynamics [2–7]. *Ab initio* work on NiTi in 2003 [6] predicted the B33 body-centered orthorhombic (BCO) phase to be the ground state, and examined energetics, relative stabilities, and details of the crystal structures of other relevant phases, namely. the B2, B19. and B19′ crystal structures. Subsequent works tried to further explain the discrepancy between the experimentally observed low-temperature martensite phase (B19′) and the calculated ground state (B33), and offered different insights on the details of martensitic phase transformation. Both B19′ and B33 structures can be seen as monoclinically distorted B19 structures, but with different monoclinic angles of about 98° and 107°, respectively. These works also offered different points of view on the high-temperature austenite phase discussed to be either the B2 structure, dynamically unstable at $T = 0$ but stable at higher temperatures (e.g., $T > 300$ K) when large enough simulation cell is used according to [4,5], or a structure with "on average" B2 symmetry behaving like a "phonon glass" according to [2,3]. Moreover, Ref. [3] utilized a generalized solid-state nudged elastic band method to obtain the minimum-energy path (MEP) from the BCO to the austenite phase (using both ideal B2 as well as phonon glass B2 structure) considering orthorhombic as well as monoclinic cells to describe the martensite phase; their Fig. 4 displays the energy of NiTi along the transformation pathway (MEP) and shows monotonic decrease from B2 to BCO. Conversely, Ref. [4] included the finite-temperature effects by performing high-accuracy *ab initio* molecular dynamics simulation based on density functional theory (DFT) combined with generalized thermodynamic integration methods; they evaluated phase stabilities of the B2, B19′, and B33 phases and the relevant transition temperatures from their free energies in the temperature range 0–900 K (results of which are shown in their Fig. 7); overall their results seem to be in good agreement with the experimental results on phase stabilities and martensitic phase transformation in NiTi.

On the other hand, while experimental studies seem to have a consensus on the structure of NiTi martensite as B19′ (and not the calculated ground-state structure B33) [8,9], different austenite structures have been reported thus far: For example, high-temperature x-ray studies of the powder samples suggest the high-symmetry B2 structure [10] while similar studies of the single crystals suggest a structure that deviates from B2 but "on average" appears to be similar to it [11]. Finally, one should also stress that multiple low-energy planar defects (e.g., twins) have been theoretically predicted as well as experimentally observed in regard to the formation of NiTi martensite [3,12,13].

*krcmarm@gvsu.edu

†morrisj@ameslab.gov

In this paper we focus on the role of stacking faults in connecting the B2 and B33 NiTi phases. Utilizing a body-centered orthorhombic (BCO) conventional cell for the B33 structure, in Sec. III below, we describe the B2 → B33 transformation in terms of stacking faults formed by alternate bilayer shifts by $\frac{1}{2}$ [100] on the $(011)_{B2}$ plane, obtaining a viable transformation pathway, and noting that the same transformation mechanism would also work for the B19 parent phase. This transformation pathway is significantly different than the traditional "shearing" pathway, for example, discussed in [6]. Having in mind that the experimentally reported martensite phase has B19′ structure with the monoclinic angle of 97.8° and that the calculated ground-state B33 structure is its special-case variant with the monoclinic angle of 107.2°, we examine the B33-like structures built from different arrangements of the stacking faults in the B19 (or B2) bilayers that essentially have monoclinic cells with monoclinic angles in the range from 98° to 102°, seeking the low-energy structures in order to suggest that the NiTi martensite might contain a range of stacking-fault variants of B19/B2 structures which appear B19′/B33-like. We find four low-energy stacking-fault variants which are energetically 5.8–8.5 meV/atom above our calculated B19′ structure that corresponds to the experimentally reported martensite, and which also have monoclinic angles in the range from 98° to 99.5°. This suggests that, at finite temperatures, these structures potentially play an important role in the NiTi martensitic phase transformation, appearing as a part of the martensite phase. Exploring further planar shifts in NiTi systems following the same line of thought, and guided by our previous work involving ductile transition metal–rare earth binary alloys [14], we seek a B27 variant of the NiTi alloy, since the B33 structure can be constructed from the B27 structure following a set of specific coordinated planar shifts [15]. We determine that it is only 1.2 meV/atom above the calculated ground-state B33 structure, thus energetically well below the B19′ structure reported experimentally as the NiTi martensite. The calculated phonons for B27 NiTi confirm that it is dynamically stable. Due to its rather low energy and geometrical connection to the B33 phase (involving coordinated planar shifts), we suggest that it might play a significant role in defining the characteristics of NiTi martensite.

II. METHODS

We perform first-principles calculations based on the density functional theory (DFT) that employ the ultrasoft pseudopotentials (USPP) method [16] within the generalized gradient approximation (GGA) [17] and with the exchange-correlation functional of Perdew and Wang [18], utilizing the VASP code [19]. We chose to employ the USPP method [rather than, say, the projector augmented wave method (PAW)] firstly for practical reasons: We have worked extensively on Ni- and Ti-based transition-metal alloys over the years, collecting numerous benchmarking calculation results relevant for this study. Secondly, our main goal was to examine relative energies among many different Ni-Ti structures and the USPP method has been proven well suited for such study, giving the results consistent with those of the PAW calculations [6]. The USPP we utilized for Ti includes the p semicore states (namely, the Ti_pv VASP potential), resulting in ten electrons included as the valence electrons; similarly, the USPP for Ni also contains ten valence electrons. The Brillouin zone integrations are performed using the Monkhorst-Pack scheme [20] with a variety of k-point meshes depending on the sizes of relevant supercells. Our calculations employ the 450-eV energy cutoff which is well above the recommended cutoff (e.g., 30% over the default parameter for a studied system) when accurate bulk relaxations are to be performed, and the convergence over the energy cutoff parameter was tested for the several most relevant structures of our interest; the cutoff is also comparable to that used in similar earlier studies [6]. The high-energy cutoff is thus chosen because of a large body of calculations that had to be performed on specific stacking-fault structures requiring large supercells as well as volume relaxations starting from rather crude initial guesses, as we built our supercells by initially adding specific layers with their original structural characteristics onto one another.

To get to the fully relaxed structures, in terms of both lattice parameters as well as ionic positions in the most pragmatic manner for these large supercells, we follow the VASP recommendation for accurate bulk relaxations utilizing parameters ISIF = 3 (to allow for volume relaxation as well as relaxation of the internal degrees of freedom) and ISMEAR = 1 (for controlling of partial orbital occupancies), while using atomic relaxation maximal force criterion of 0.01 eV/Å. Upon establishing correct lattice parameters and atomic placements within our supercells, we carry out final high-accuracy total energy calculations by performing a final self-consistent run with ISMEAR = −5: While fixing the volume/lattice parameters and the ionic placements we fully converge electronic degrees of freedom, obtaining the final energy for each stacking-fault structure we consider. Finally, in order to investigate dynamical stability of the selected low-energy stacking-fault structures and of the B27 structure that closely competes in energy with the B33 structure, we use the PHONOPY package [21] to obtain their phonon spectra and their free energies.

III. PATHWAYS TO STACKING FAULTS AND TO B33 STRUCTURE, AND ALTERNATE STRUCTURES AND THEIR ENERGETICS

A. Transformation pathways from the B2 (CsCl) crystal structure to the B33 (body-centered orthorhombic CrB) crystal structure

Beginning by briefly reviewing geometrical relationships among the relevant NiTi structures, namely, B2, B19, B19′, and B33, we note that they are compellingly presented in Fig. 1 of Ref. [6]. The B2 structure has a two-atom simple cubic primitive cell, and a doubled B2 cell with tetragonal symmetry can be built from the B2 vectors [100], [011], and [01$\bar{1}$]. Four-atom B19 structure can be obtained by orthorhombic distortion of the doubled B2 cell, accompanied with the atomic shuffles. The B19′ structure is obtained by monoclinic distortion of the B19 cell, accompanied with further atomic shuffles. Finally, the B33 cell is a higher-symmetry variant of the B19′ four-atom primitive cell with monoclinic tilt angle γ such that $\cos(\gamma) = -a_{B19'}2b_{B19'}$,

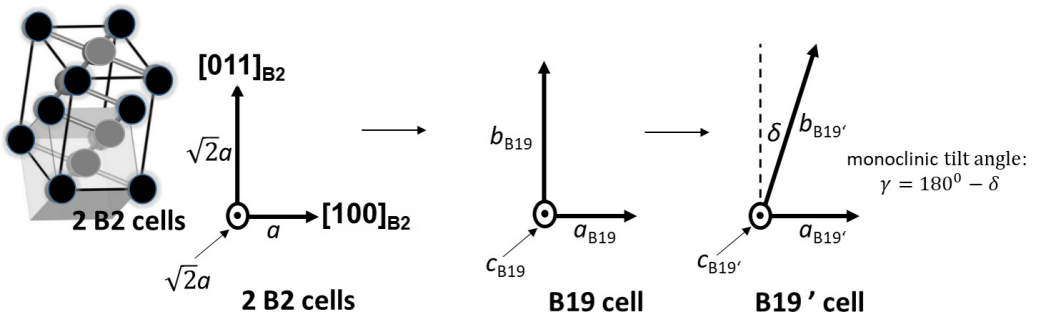

FIG. 1. Three-dimensional sketch of a B2 structure formed from two primitive cells ("2B2"), together with the sketches of lattice vectors for 2B2, B19, and B19′ cells. Depicted cells each contain four Ni and Ti atoms.

where $a_{B19'}$ and $b_{B19'}$ are lattice constants; the B33 structure can also be represented as an eight-atom body-centered orthorhombic (BCO) conventional cell such that their a and c lattice constants coincide, whereas their b lattice constants satisfy the following relationship: $b_{BCO}/2b_{B19'} = \sin(\gamma)$. Also, the B19′ structure has an obtuse γ angle. At a particular choice of γ, the shear moves the top plane of the unit cell by one periodicity along the shift direction, generating a BCO structure. A simplified geometrical sketch of the formation of these structures is shown in Fig. 1. We note that the conventional description of the B2 → B33 transformation (as special case of B2 to B19′ transformation) is similar to B19 to B33 (or B19′) transformation: Shearing of the lattice along the $[100]_{B2}$ direction produces the B19′ phase with the experimentally observed 98° angle for NiTi.

We first carried out benchmarking calculations, the results of which are shown in Table I, together with the corresponding results reported in Ref. [6]. For simplicity, we omit listing all the atomic positions due to the atomic shuffles within the unit cells, but we note that they and the lattice parameters are in very good agreement with the other published results such as those in Ref. [6].

We next examine an alternate approach to the B2 → B33 (or B19→B33) structural phase transformation. For simplicity, we adopt the assumption that the NiTi austenite structure is the B2, even though zero-temperature *ab initio* calculations show that it is dynamically unstable. This is, however, the high-temperature NiTi phase, and recent work [4,5] which considers finite-temperature effects showed that this phase is stabilized by the entropic effects at temperatures above ∼300 K. The consideration of the alternate B19 phase is trivial, as the stacking-fault treatment is identical. Rather than introducing a tilt, as described in Fig. 1 or Fig. 2(a), we introduce shifts of pairs of $(011)_{B2}$ planes, as indicated in Fig. 2(b). We consider arbitrary shifts below, introducing alternate bilayer stacking faults by $\frac{1}{2}$ [100] on the $(011)_{B2}$. Continued shearing would eventually reform the B2 phase. The depiction of this comparison is shown in Fig. 2. In other words, the B33 structure has a close relationship to $(011)_{B2}$ or $(001)_{B19}$ stacking faults. For easier visualization of the atomic positions, we note that between each nearest neighbor pair of the front (back) gray atoms located along the $[100]_{B2}$ direction is a single back (front) red atom; as one moves along the $[011]_{B2}$ direction, the location of both gray and red subsequent atoms alternates from front (back) to back (front) locations. More detail on the locations of atoms and the directions of their shuffles along the transformation pathway from B2 to B33 structure can be found in the Appendix, where we present two-dimensional (2D) figures of the relevant atomic planes accompanied with the corresponding "three-dimensional (3D)"/oblique figures of supercells used to calculate energies along the pathway.

A stacking fault may be created by a shift of a bicrystal by $\frac{1}{2}$ [100] on the $(011)_{B2}$ or $(001)_{B19}$ plane; a regular array of such faults creates the B33 phase in a very similar manner for either for B2 or B19 parent phases. A depiction of the stacking-fault structures relevant to the B33 phase is shown in Fig. 3.

The transformation may thus occur by alternate displacements of paired layers, and a particular displacement, which

TABLE I. Comparison of our *ab initio* results on lattice parameters and energetics of the relevant structures relative to the energy of B2 structure ($E - E_{B2}$ in eV/atom) with the results of Ref. [6].

Lattice parameters (Å)	B2	B19	B19′	B33 (BCO cell)	B33 (B19′ cell)
This work	$a_{B2} = 3.021$	$a_{B19} = 2.748$ $b_{B19} = 4.626$ $c_{B19} = 4.184$	$a_{B19'} = 2.920$ $b_{B19'} = 4.680$ $c_{B19'} = 4.050$ $\gamma = 98^\circ$	$a_{BCO} = 2.960$ $b_{BCO} = 9.443$ $c_{BCO} = 4.006$ $\gamma = 90^\circ$	$a_{B33} = 2.960$ $b_{B33} = 4.948$ $c_{B33} = 4.006$ $\gamma = 107.4^\circ$
$E - E_{B2}$	0	–0.030	–0.041	–0.050	–0.050
Ref. [6] (USP-GGA)	$a_{B2} = 3.009$	$a_{B19} = 2.776$ $b_{B19} = 4.631$ $c_{B19} = 4.221$	$a_{B19'} = 2.292$ $b_{B19'} = 4.684$ $c_{B19'} = 4.048$ $\gamma = 97.8^\circ$	$a_{BCO} = 2.940$ $b_{BCO} = 9.431$ $c_{BCO} = 3.997$ $\gamma = 90^\circ$	$a_{B33} = 2.940$ $b_{B33} = 4.936$ $c_{B33} = 3.997$ $\gamma = 107.2^\circ$
$E - E_{B2}$	0	–0.027	–0.042	–0.050	–0.050

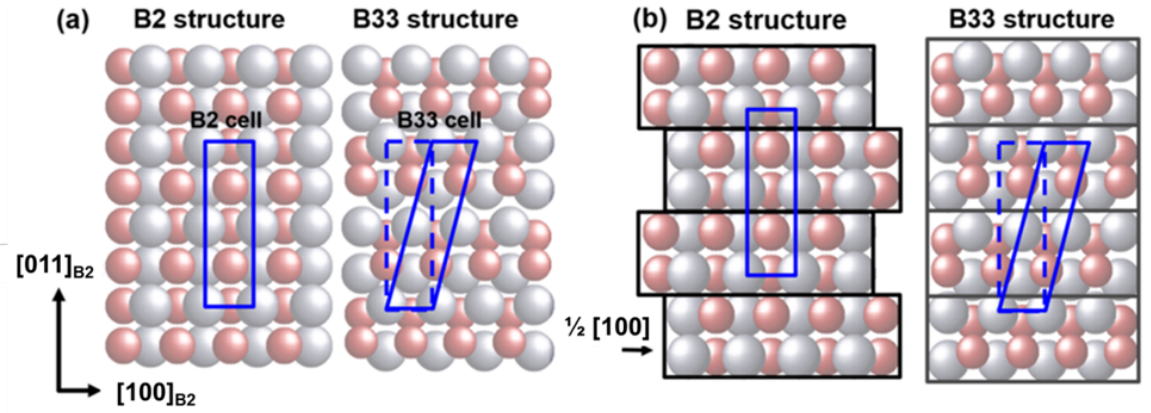

FIG. 2. (a) B33 cell obtained by shearing the 2 B2 (or B19) cell and relaxing the structural degrees of freedom; (b) B33 cell obtained by introducing alternate bilayer stacking faults by $\frac{1}{2}$ [100] on the $(011)_{B2}$ or by ($\frac{1}{2}$ [100] on the $(001)_{B19}$).

becomes the B33 phase. This mechanism requires no net shear. It should also result in dissociation of $b = [100]$ dislocations into $\frac{1}{2}$ [100] partials. Such dissociations have been observed in the low-temperature phase of NiTi [8]. This immediately suggests the existence of low-energy defect structures of the B33 phase associated with disordered arrangement of stacking faults, which has been seen in ZrCu [22–24], ZrIr and ZrRh [25], and ZrCo [26]. Moreover, slip of dislocations with ⟨110⟩ and/or ⟨111⟩ Burgers vectors fund in CoTi and ZrCo have been attributed to improved ductility in these B2 alloys [27]. For NiTi we will focus on the stacking-fault structures after showing the energetics of the B2 → B33 structural phase transformation along this viable transformation pathway, and compare these results with some previous works.

To obtain energetics of the transformation along our discussed transformation pathway, we freeze-in the relevant displacement of pairs of atomic planes along the pathway, and relax all other structural degrees of freedom. For the reference energy, we take that of the B2 structure shown in Fig. 2; thus all atoms are placed on their ideal B2 positions (in other words, no symmetry-breaking shuffles are introduced in B2). The result is shown in panel (a) of Fig. 4. The curve exhibits a clear decreasing trend along the entire pathway. Note that a dashed line is used between the point corresponding to B2 and the first point along the pathway to indicate that the steepness of the curve is not in fact linear, due to the breaking of symmetry as soon as one displaces even by a very small amount along the transformation pathway. By symmetry, the slope at zero displacement must be zero. Overall, no transformation barrier is found along this pathway.

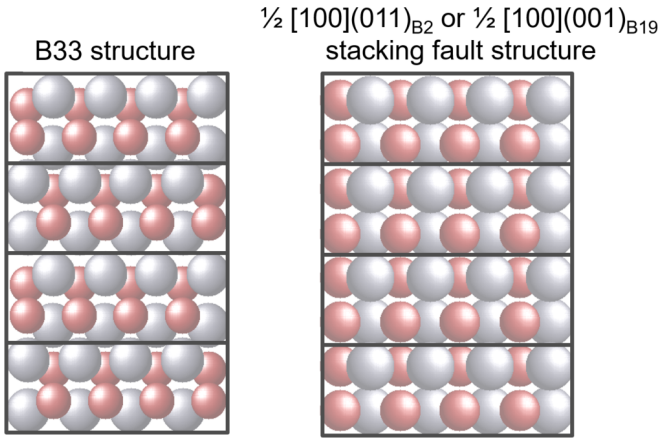

FIG. 3. Comparison of the B33 phase shown as BCO structure with the (unrelaxed) array of pairs of alternate $\frac{1}{2}$ [100] on the $(011)_{B2}$ or $(001)_{B19}$ stacking faults.

The solid line in Fig. 4(b) shows the energetics along the transformation pathway for the B19 → B33 structural transformation, relative to the energy of our calculated B19 structure. The added dashed line displays the "gamma plot" calculation, where we only allow uniform relaxation of the atomic planes in the direction perpendicular to the plane of stacking faults, as opposed to allowing all relaxations (particularly the "shuffles" related to the *N*-point phonon). Similarly to B2, the solid curve shows no transformation barrier, and no abrupt changes in curve steepness along the transformation pathway, since the B19 structure already incorporates atomic shuffles which play a significant role in the transformation to B33. The gamma plot indicates the energy of formation of planar defects along the transformation pathway, such that the final structure is B33-like, since in-plane B19 lattice parameters are frozen in; obviously, forming these planar-fault structures in the B19 phase lowers the energy up to 0.01 eV/atom, according to our calculations.

The result shown in Fig 4(a) can be compared with the results of Ref. [6] [in particular, their Fig. 2(a)], where the B33 phase was obtained through shearing of the parent structure from the undistorted B2 structure (represented in a B19′ cell) and relaxing all other structural degrees of freedom, thus allowing for atomic shuffles as well as monoclinic distortion of the original cell; this result indicates transition to B33 (monoclinic angle of ∼107°) without a barrier and is consistent with dynamical instability of the calculated B2 phase. Some more recent studies also examined the austenite-to-martensite phase transformation in NiTi [3,4].

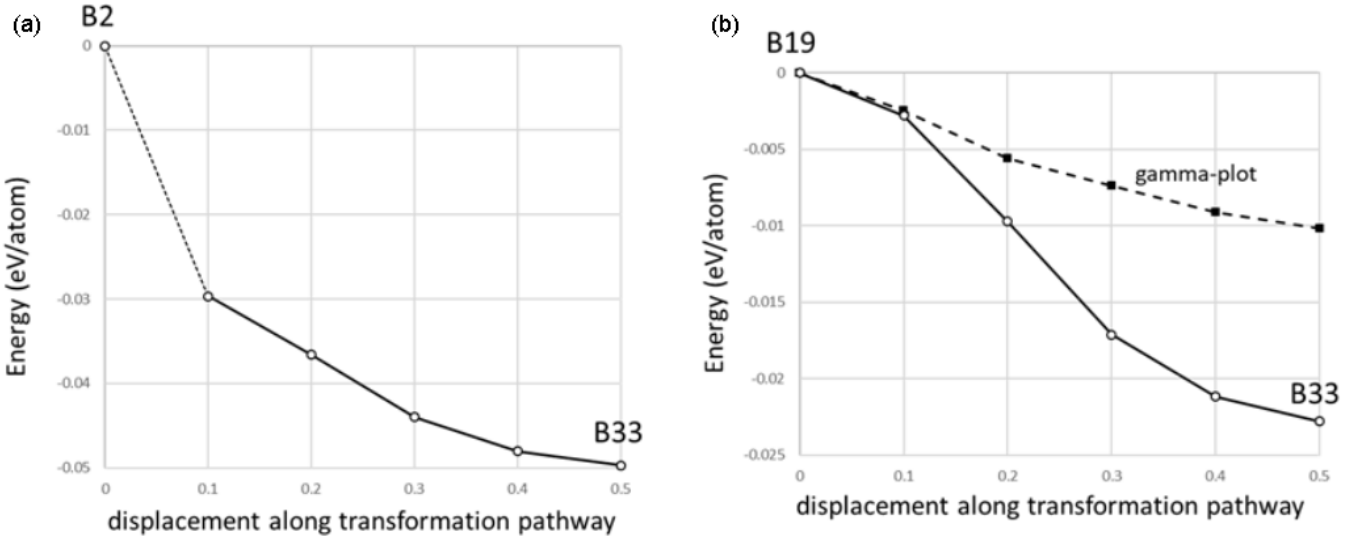

FIG. 4. (a) Energetics of the B2 → B33 transformation along the pathway shown in Fig. 2, with incremental shifts of alternate bilayers along the transformation pathway represented on the horizontal axis. (b) Energetics of the B19 → B33 transformation along the transformation pathway; also shown for comparison is the corresponding gamma plot.

B. Alternate competing crystal structures based on periodic stacking faults

In the previous section, we describe the B33 crystal structure in terms of a periodic array of stacking faults on the $\{110\}_{B2}$ planes. This suggests a series of potential competing crystal structures, formed by alternate arrangements of these stacking faults. Here, we examine alternate NiTi stacking structures and their energetics, which can be seen as variants of B19 or B33 structures (built from the B19-like or B2-like monolayers) that possess periodic stacking faults. We denote these alternate structures as $m+n$ in terms of the numbers of $\{110\}$B2 layers between stacking faults, such that there are n layers shifted by $\frac{1}{2}$ [100]B2 and m layers unshifted, forming a crystal structure that is $m+n$ layers in total. In this representation, the B33 phase is a 2+2 structure, and Fig. 5 demonstrates a 4+2 structure. Compared to B33, the alternate structures have larger unit cells as shown in Fig. 5, which can be represented as monoclinic cells with effective tilt angles lower than that of the B33 NiTi phase (see the boldface boundary shapes in Fig. 5). They are of interest to us exactly because of the tilt angle closer to the one found experimentally

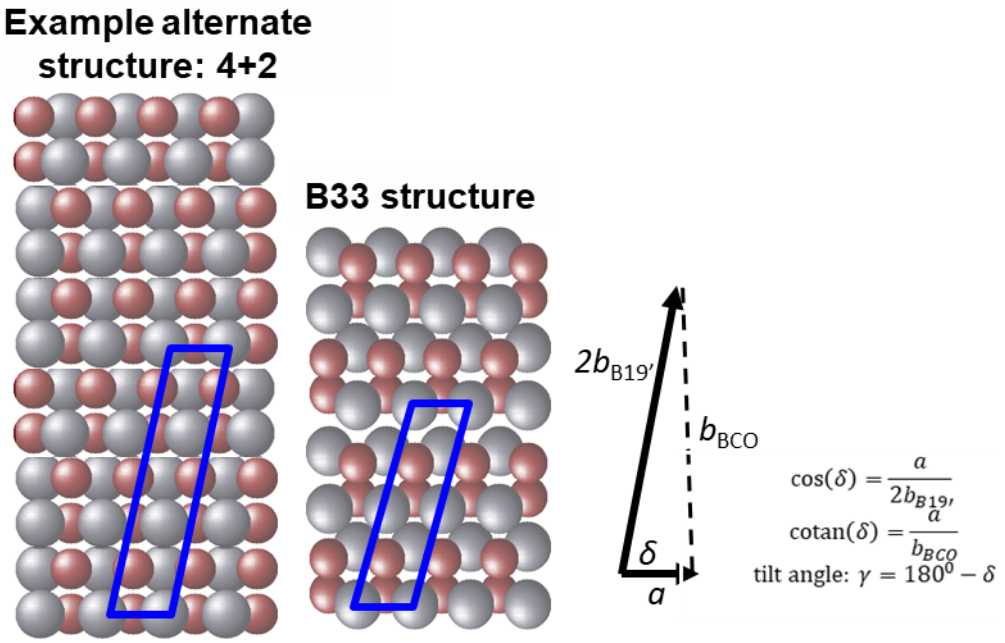

FIG. 5. Example alternate stacking structure 4+2 obtained by combining B19-like monolayers and two monolayers shifted by $\frac{1}{2}$ [100] on the $(001)_{B19}$ and relaxing all structural degrees of freedom (the B33 structure is included for comparison); also shown is how the tilt angle can be calculated for the B33 phase, and similarly for the alternate stacking structure.

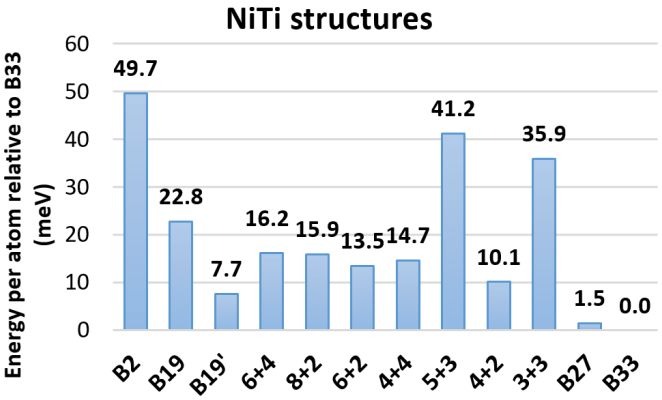

FIG. 6. Energy (in meV/atom) of calculated NiTi structures relative to that of the B33 phase.

for the NiTi martensite (recall the monoclinic B19′ phase with the tilt angle of 98°).

The energetics of the alternate structures (together with other relevant NiTi phases) are summarized in Fig. 6, whereas Fig. 7 shows the effective tilt angle for the structures together with their energies relative to that of the B33 ground state. The figures show that we found several low-energy structures, namely, 4+4, 6+2, 6+4, and 8+2, with energies ranging from 5.8 to 8.5 meV/atom above that of the calculated B19′martensite phase, which coincidentally also have effective tilt angles of about 98° and 99°, thus very close to the one found for the NiTi martensite. (We also tried odd values of m and n; however, this always resulted in significantly higher energies.) This opens a possibility that, at finite temperatures

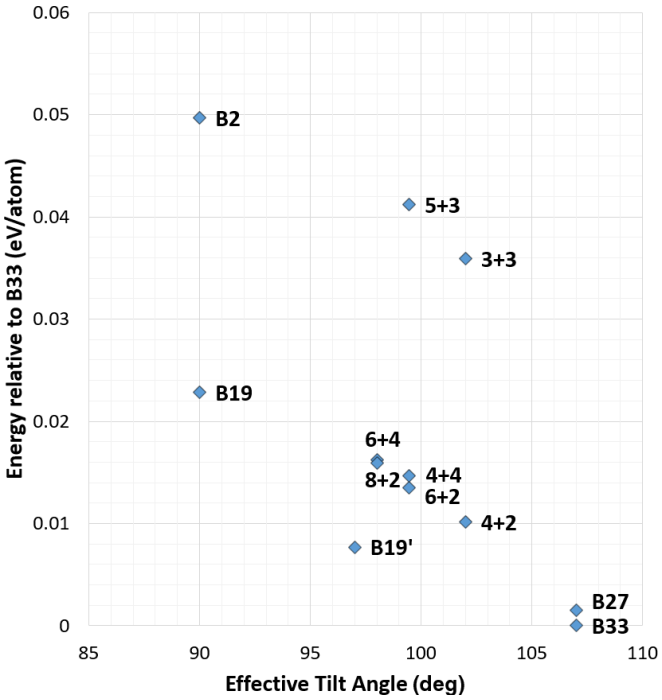

FIG. 7. Energy (in eV/atom, relative to the energy of the B33 phase) of the examined NiTi structures vs their effective tilt angle (in degrees).

where entropic effects play a role, these alternate stacking structures could become a common occurrence. [Note that we also calculated 8+4 and 10+2 structures (not included in Figs. 5 and 6) which have tilt angles closest to 97° and are found to be 17.2 and 17.5 meV/atom above the B33 energy.]

C. Energetics of NiTi in the competing B27 (FeB) crystal structure

Several ductile rare earth–transition metal (RM) binary alloys with B2 structure have also been found to exhibit B27 crystal structure. (The B27 prototype structure is FeB, its Pearson symbol is oP8, and its space group is *Pnma*, which corresponds to an eight-atom orthorhombic primitive cell [28].) The YCu alloy, being one composition that undergoes a B2→B27 transition, has been discussed in Ref. [14]. The significant ductility of NiTi together with its B2 high-symmetry structure points to the similarity with the B2 RM systems. Moreover, as discussed in Ref. [15], the B33 structure can be obtained from the B27 structure through a volume-conserving transformation involving coordinated planar shifts in the B27 lattice (see Fig. 8 for details). Finding that NiTi exhibits a tendency to stacking faults, and due to the known close competition between B33 and B27 structures in related systems, we suspect that the B27 structure might also be a competitive crystal structure for the NiTi system. Using the lattice parameters of B27 YCu as an initial guess, we fully optimize the NiTi-based B27 structure, minimizing the energy with respect to the cell volume, and relaxing all the internal degrees of freedom. In our calculations we do not initially impose the condition of equality of volumes between the B33 and B27 structures, and we find that the lowest-energy B27 NiTi structure has primitive cell volume that is, within 0.6%, consistent with the volume of the eight-atom BCO/B33 NiTi cell. (Details on the lattice parameters and internal degrees of freedom for the B27 primitive cell can be found in the Appendix.) We use our results to construct Fig. 8, displaying the exact geometrical relationship between the B33 and B27 NiTi phases. What is most surprising about this B27 NiTi phase is that it is only 1.2 eV/atom higher in energy than the calculated ground-state B33 structure. This means that the B27 structure might appear as a part of NiTi martensite and play a role in the martensitic phase transformation.

It is important to note that the calculated B27 structure appears to be closer in energy to the calculated ground-state B33 structure than the next most-stable calculated NiTi structure that can be currently found in the literature [29]: This low-energy NiTi has B19′ structure and is 0.002 eV/atom higher in energy than B33; it has space group $P2_1/m$, while the B27 structure has space group *Pnma* with the primitive cell which is about twice the volume of the calculated B19′ structure of Ref. [29]. However, it is even more important to emphasize that the low-energy B19′ structure reported in Ref. [29] has been found by using the PAW method, and energy cutoff of 520 eV. Since this low-energy structure differs from our calculated B27 structure by less than 1 meV while being found by a different type of *ab initio* calculation, more extensive study of the relative stability of these two structures by the same *ab initio* approach is needed to conclude which of the

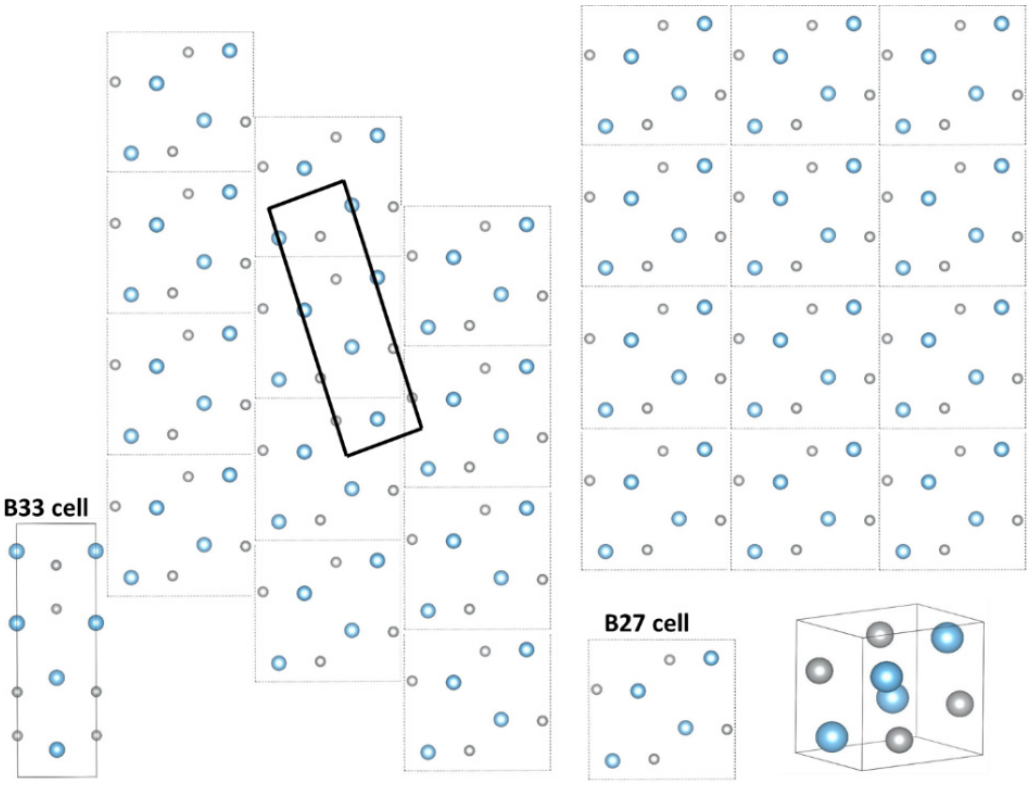

FIG. 8. Calculated B33 and B27 eight-atom cells are used in order to show mutual geometrical relationship between the B33 and B27 structures.

two is more stable/closer in energy to the ground-state B33 structure.

Finally, in order to investigate dynamical stability of the B27 NiTi phase, we calculate its phonon spectrum utilizing the PHONOPY code [21]. The result is shown in Fig. 9, where we also show the B33 phonon spectrum for reference and comparison. It can be seen that NiTi B27 is indeed dynamically stable (i.e., without any imaginary phonon frequencies), and that its phonon spectrum exhibits many features similar to those of NiTi B33. We note that the BCO cell was used to find the phonon spectrum for B33, allowing the most straightforward comparison with the spectrum of the orthorhombic B27 NiTi. We also note that the B33 NiTi phonons have been reported in Ref. [4], where the authors utilized the B19′-based structure in order to compare the phonons of both the experimentally determined martensitic phase B19′ and the calculated ground-state phase B33. Due to the difference in the Brillouin zones corresponding to the BCO structure used here and the B19′-like structure used in Ref. [4], direct comparison of the two results is not possible. However, the two calculations should agree in their prediction of the maximal phonon frequency in the B33 phase. Comparing their Fig. 10(c) and the left panel of our Fig. 9, the calculated maximal frequencies appear to be in very good agreement.

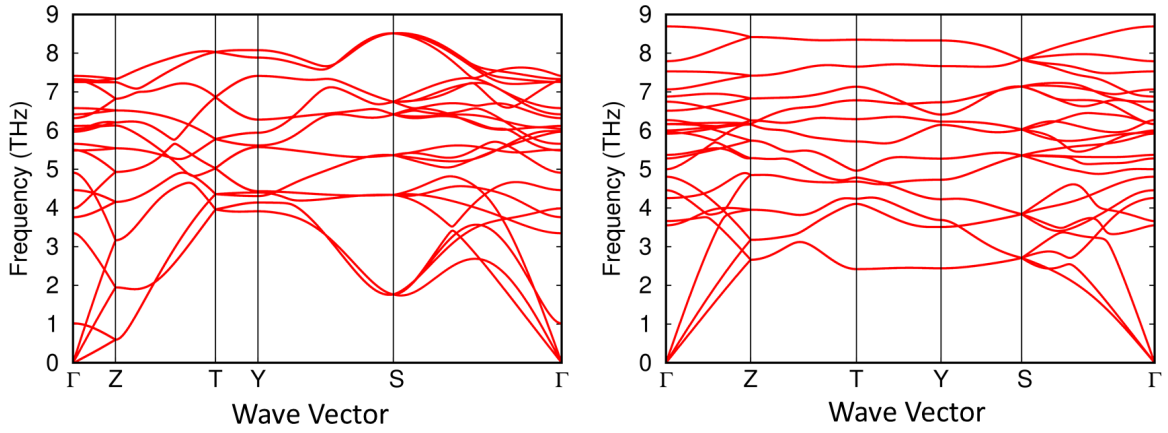

FIG. 9. Phonon spectra for B33 (left panel) and B27 (right panel) NiTi structures obtained by the PHONOPY code [21].

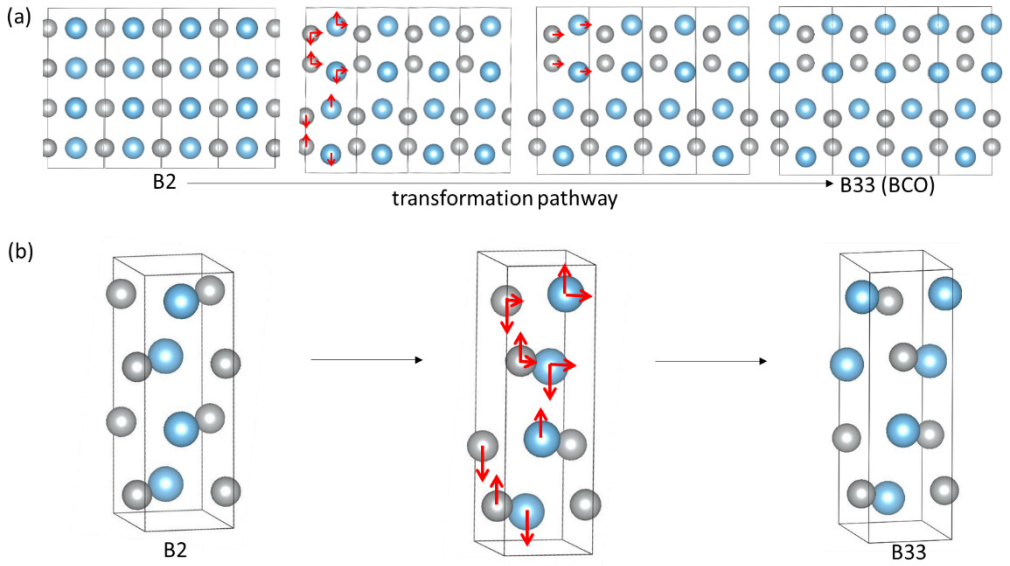

FIG. 10. (a) Two dimensional representation of the transformation from B2 to B33, projected along the direction. Red arrows indicate direction of motion. (b) Three dimensional representation of the unit cells shown in (a) with corresponding shifts.

Given the B33–B27 energy difference and the phonon dispersions (or phonon density of states), one may estimate the phonon contribution to the free energy, and thereby predict a temperature where one may expect a B33-B27 transition. This is evaluated and discussed in Appendix 3. There are issues with evaluating the accuracy of this temperature, as discussed in that section, and the B33-B27 transition has not been observed to our knowledge, presumably precluded by the other transformations.

IV. DISCUSSION

It has already been recognized that planar defects (e.g., twins) play a very important role in defining the NiTi martensite, as the results of both theoretical [3,13] and experimental [12] studies suggest. However, there are many competing binary Ni-Ti structures that have not been considered or discussed to date: In particular, these are the structures with periodic planar defects, thus larger unit cells that are produced via alternate stacking of the Ni-Ti monolayers. As Fig. 7 demonstrates, these larger structures are rather close in energy to the calculated B19′ martensite, and their cells correspond to smaller monoclinic angles, so compared to the B33 structure, they are much closer to the monoclinic angle of the experimentally determined B19′ NiTi martensite. Due to the similarity of the B19-like and B33-like bilayers in the variety of low-energy structures that contain periodic planar defects, and their similarity to the B19′ structure, it is very likely that resolving the exact martensite structure in experiments is a very complex task. The effect of stacking faults in obscuring the ground-state structure has been noted in the chemically similar CoZr system [26].

We also demonstrate that energetically, the B27 structure is very closely competing with the B33 phase. Since correlated planar shifts of subcrystals of this structure create the crystal of the other (namely, B33), it is likely that there exist many competing variants that incorporate B27 structure and its periodic stacking faults leading toward the B33 structure. Such structures could thus also appear as integral parts of the NiTi martensite, and making a distinction among these various structures in NiTi at low temperatures would be rather challenging.

We note that the stacking faults discussed here could play an important role in the mechanical properties of NiTi and related materials. The stacking faults should lead to dissociated dislocations, and this has been observed in NiTi. Indeed, the dissociations would provide a natural place for the B2→B33 phase transition to initiate. The close competition between the B2, B27, and B33 phases is not unique to this system, but is also observed in the ductile rare-earth/metal alloys such as YAg and YCu [14], as well as TiCo, ZrCo, and ZrPd alloys [26]. All of these alloys show significant ductility in the B2 phase, despite their high degree of chemical order, and the "traditional" understanding that highly ordered B2 structures have limited deformation modes, leading to brittle behavior. We suggest that the combined behavior of the dissociated dislocations and associated phase transformations contribute to the ductility in these materials.

The competition between the different pathways from B19 to the B33 body-centered orthorhombic (BCO) phase, indicated by Figs. 1 and 2, may have implication for the understanding of microstructures formed during the transition, including both twinning geometries and habit plane. The pathway indicated by Fig. 1 corresponds to a shear deformation, coupled to a "shuffle" (a static displacement corresponding to a phonon mode with finite $|\mathbf{q}|>0$) mode. This is the first type of transformation described in the classic Wechsler-Lieberman-Read (WLR) paper [30], in which no net slip occurs. In contrast, the pathway shown in Fig. 2 is explicitly in terms of slip along the planes of the parent/product phases, corresponding to the second type described in WLR. Moreover, while the transformation associated with Fig. 1 suggests a rotation of one of the lattice vectors during the transformation process, the transformation pathway in Fig. 2 preserves the direction

of all lattice vectors during the transformation process. There are further, related implications to Landau theory treatments of the transformation: The process shown in Fig. 1 essentially is a special case of the B19→B19′ transformation [31], coupling the shear to the associated phonon modes. However, as noted in [6], continued shearing beyond the formation of the B33 actually reverses the pathway, leading back to the B2 phase. Similarly, the slips indicated in Fig. 2 can be continued to return to the B2 phase. In such cases, there is not a group-subgroup relationship as typically expected in a Landau description, and the expansions such as those in [31] do not capture this. Thus a more complete treatment [32,33] would be required. This may further present an opportunity to create desired grain boundary microstructures [34].

V. SUMMARY

First-principles calculations are used to show that NiTi stacking faults can be utilized to describe the B2 → B33 phase transformation: alternate bilayer shifts by $\frac{1}{2}$ [100] on $(011)_{B2}$ planes will produce the B33 phase from the B2 or the B19 phase. Using B19 (or B2) bilayers, one can build a variety of stacking-fault structures which are B33-like, but possess monoclinic tilt angles very close to that experimentally observed in the B19′ NiTi martensite; these are low-energy stacking-fault structures, and may thus appear within the martensite phase and/or play a role in the NiTi martensitic phase transformation. Calculations confirm our hypothesis that the B27 crystal structure could closely compete with the B33 structure energetically, similar to ductile binary alloys with a high-temperature B2 structure. We find the dynamically stable, low-energy B27 NiTi phase to be only 1.2 meV/atom higher in energy than the calculated B33 ground state. Since the B27 phase can be connected with the B33 via a specific sequence of coordinated planar shifts of the underlying subcrystals, we propose that this phase as well, together with many B19/B33-like variants with periodic stacking faults, might be an integral part of the NiTi martensite phase.

The Department of Energy will provide public access to these results of federally sponsored research in accordance with the DOE Public Access Plan [35].

ACKNOWLEDGMENTS

J.R.M. was supported by the US Department of Energy Office of Science, Basic Energy Sciences, Materials Sciences and Engineering Division. G.D.S. acknowledges support from the Energy Dissipation to Defect Evolution (EDDE), an Energy Frontier Research Center funded by the US Department of Energy, Office of Science, Basic Energy Sciences under Contract No. DE-AC05-00OR22725.

APPENDIX

1. Two- and three-dimensional representation of the NiTi structural transformation from B2 to B33 structure

See Fig. 10. Panel (a) begins with the B2 planes spanned by the vectors [100] and [011], and ends with the planes spanned by the vectors [100] and [001] of the final B33/BCO structure. In between, atomic shuffles of the atoms within the cells are denoted by red arrows. It can be seen that the bottom two rows of atoms undergo only vertical shuffles along the transformation pathway, whereas the atoms in the top two layers undergo some vertical shuffles while overall shifting horizontally across the distance comparable to half of the lattice parameters in the [100] direction (of either B2 or BCO structure). Panel (b) shows actual spatial distribution of atoms in the "three-dimensional"/oblique supercells utilized in our calculations for the three structures: B2, BCO, and the intermediate structure halfway along the transformation pathway; vertical red arrows indicate directions of relatively small atomic shuffles whereas the horizontal red arrows indicate direction of the displacements of atoms (in the top two layers) along the B2 to B33 transformation pathway.

2. NiTi B27 structural (lattice) parameters

Calculated lattice constants for the B27 orthorhombic primitive unit cell:

$$a = 5.352\,05\ \text{Å}, \quad b = 4.077\,48\ \text{Å}, \quad c = 5.098\,63\ \text{Å}.$$

Atomic positions within the B27 eight-atom primitive cell [28]:

$$\pm x_{1,2} a\hat{x} \pm 0.25 b\hat{y} \pm z_{1,2} c\hat{z}\ (1\text{ for Ni},\ 2\text{ for Ti}),$$
$$[0.5 - (\pm x_{1,2})]a\hat{x} - (\pm 0.25)b\hat{y} + (0.5 \pm z_{1,2})c\hat{z}.$$

Calculated parameters measuring atomic shuffles for NiTi B27 structure:

$$x_1 = 0.055\,10,\ z_1 = 0.644\,24(\text{for Ni}), \quad \text{and}$$
$$x_2 = 0.163\,27,\ z_2 = 0.132\,58\ (\text{for Ti}).$$

3. Quasiharmonic approximation calculation for B33 and B27 free energies

Given the $T = 0$ K energy difference E_{B33}–E_{B27}, and the phonons shown in Fig. 9, one can estimate the phase transformation temperature between these phases. While not the

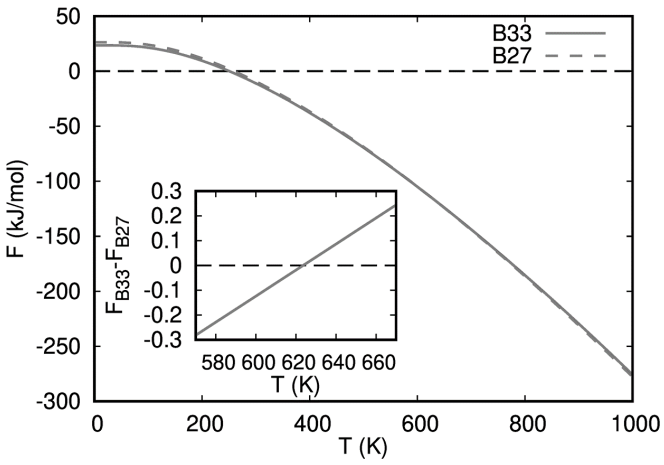

FIG. 11. Free energy and the free energy difference for the calculated B33 and B27 structures found by using QHA and PHONOPY code. Insert is showing that their free energy difference changes sign near 600 K.

major point of this paper, we present a simple estimate of this temperature here. We use quasiharmonic approximation (QHA) in order to calculate B33 and B27 free energies as the functions of temperature, and compare them. As shown in the inset of Fig. 11, we find that their difference changes sign at a rather high temperature of about 620 K. At this temperature, these phases are not likely to be relevant due to the other transitions that preclude this one. We note that some caution should be used in this: There are uncertainties in the free energies, due to a number of issues. First, the phonons are likely slightly sensitive to the details of the energy functional used in the DFT calculations. Secondly, the phonons are undoubtedly sensitive to lattice expansion, a major source of anharmonicity in most systems, and this is not fully accounted for. Third, NiTi is known to have phonon anomalies, associated with the phase transformations [4,31], indicating further the importance of anharmonic contributions that may not be fully described by the quasiharmonic expansion. Finally, the calculated transition temperature is extremely sensitive to small errors in the free energies of the different phases, as has been demonstrated for both model solid-solid phase transformations where quasiharmonic approaches have been tested [36], and for other first-order phase transformations such as melting [37].

[1] Y. Y. Ye, C. T. Chan, and K. M. Ho, Phys. Rev. B **56**, 3678 (1997).
[2] N. A. Zarkevich and D. D. Johnson, Phys. Rev. B **90**, 060102(R) (2014).
[3] N. A. Zarkevich and D. D. Johnson, Phys. Lett. **113**, 265701 (2014).
[4] J. B. Haskins, A. E. Thompson, and J. W. Lawson, Phys. Rev. B **94**, 214110 (2016).
[5] J. B. Haskins and J. W. Lawson, J. Appl. Phys. **121**, 205103 (2017).
[6] X. Huang, G. J. Ackland, and K. M. Rabe, Nat. Mater. **2**, 307 (2003).
[7] S. Kadkhodaei and A. van de Walle, Acta Mater. **147**, 296 (2018).
[8] Y. Kudoh., M. Tokonami, S. Miyazaki, and K. Otsuka, Acta Metall. Mater. **33**, 2049 (1985).
[9] G. M. Michal and R. Sinclair, Acta Crystallogr., Sect. B **37**, 1803 (1981).
[10] M. J. Marcinkowski, A. S. Sastri, and D. Koskimaki, Philos. Mag. **18**, 945 (1968).
[11] F. E. Wang, W. J. Buehler, and S. J. Pickart, J. Appl. Phys. **36**, 3232 (1965).
[12] K. Otsuka and X. Ren, Prog. Mater. Sci. **50**, 511 (2005).
[13] P. Sesták, M. Cerny, and J. Pokluda, Intermetallics **19**, 1567 (2011).
[14] J. R. Morris, Y. Ye, Y.-B. Lee, B. N. Harmon, K. A. Gschneidner, and A. M. Russell, Acta Mater. **52**, 4849 (2004).
[15] D. Hohnke and E. Parthe, Acta Crystallogr. **20**, 572 (1966).
[16] D. Vanderbilt, Phys. Rev. B **41**, 7892 (1990).
[17] J. P. Perdew and Y. Wang, Phys. Rev. B **33**, 8800 (1986).
[18] J. P. Perdew and Y. Wang, Phys. Rev. B **45**, 13244 (1992).
[19] G. Kresse and J. Hafner, Phys. Rev. B **48**, 13115 (1993); G. Kresse, and J. Furthmuller, Comput. Mater. Sci. **6**, 15 (1996); Phys. Rev. B **54**, 11169 (1996).
[20] H. J. Monkhorst and J. D. Pack, Phys. Rev. B **13**, 5188 (1976).
[21] A. Togo, PHONOPY package, https://atztogo.github.io/phonopy (2009).
[22] J. W. Seo and D. Schryvers, Acta Mater. **46**, 1165 (1998); **46**, 1177 (1998).
[23] D. Schryvers, G. S. Firstov, J. W. Seo, J. Van Humbeeck, and Y. N. Koval, Scr. Mater. **36**, 1119 (1997).
[24] S. H. Zhou and R. E. Napolitano, Scr. Mater. **59**, 1143 (2008).
[25] R. M. Waterstrat, J. K. Stalick, X. Meng-Burany, A. E. Curzon, and M. A. Estermann, Scripta Metall. Mater. **33** (5), 695 (1995).
[26] A. François and P. Veyssière, Intermetallics **2**, 9 (1994).
[27] R. P. Mulay and S. R. Agnew, Acta Mater. **60**, 1784 (2012).
[28] http://aflowlib.org/CrystalDatabase/AB_oP8_62_c_c.FeB.html.
[29] https://materialsproject.org/materials/mp-603347/.
[30] M. S. Wechsler, D. S. Lieberman, and T. A. Read, Trans. AIME **197**, 1503 (1953).
[31] G. R. Barsch, Mater. Sci. Forum **327-328**, 367 (2000).
[32] P. Toledano, K. Knorr, L. Ehm, and W. Depmeier, Phys. Rev. B **67**, 144106 (2003).
[33] K. Bhattacharya, S. Conti, G. Zanzotto, and J. Zimmer, Nature **428**, 55 (2004).
[34] Y. Gao, Y. Zhang, B. W. Beeler, and Y. Wang, Phys Rev. Mater. **2**, 073402 (2018).
[35] http://energy.gov/downloads/doe-public-access-plan.
[36] J. R. Morris and K. M. Ho, Phys. Rev. Lett. **74**, 940 (1995).
[37] X. Song and J. R. Morris, Phys. Rev. B **67**, 092203 (2003).